




SCIENCE RESULTS

Understanding the inner structure of accretion disk in GX 17+2: AstroSat's outlook

K. SRIRAM^{1,*} , P. CHIRANJEEVI¹, S. MALU¹ and V. K. AGRAWAL²

¹Department of Astronomy, Osmania University, Hyderabad 500 007, India.

²Space Astronomy Group, ISITE Campus, U R Rao Satellite Center, Bangalore 560 037, India.

*Corresponding Author. E-mail: astrosriram@yahoo.co.in

MS received 3 November 2020; accepted 6 March 2021

Abstract. We performed the timing and spectral studies of a Z source GX 17+2 observed from AstroSat LAXPC instrument. Cross-Correlation Function (CCF) was performed using soft (3–5 keV) and hard (16–40 keV) X-ray bands across the hardness intensity diagram and found correlated/anti-correlated hard and soft lags which seems to be a common feature in these sources. We performed spectral analysis for few of these observations and found no consistent variation in the spectral parameters during the lags, however 10–40% change was noticed in diskbb and power-law components in few of observations. For the first time, we report the detection of HBOs around ~ 25 Hz and ~ 33 Hz along with their harmonics using AstroSat LAXPC data. On comparison with spectral results of HB and other branches, we found that inner disk front is close to the last stable orbit and as such no systematic variations are observed. We suggest that the detected lags are readjustment time scales of corona close to the NS and constrained its height to be around few tens to hundreds of km. The detected lags and no significant variation of inner disk front across the HID strongly indicate that structural variation in corona is the most possible cause of Z track in HID.

Keywords. Accretion—accretion disk—binaries: close—stars: individual (GX 17+2)—X-rays: binaries.

1. Introduction

Neutron Star (NS) Low Mass X-ray Binaries (LMXBs) that are highly luminous (close to or more than Eddington luminosity) exhibiting a Z-shaped track on the Hardness Intensity Diagram (HID)/Colour–Colour Diagram (CCD) are termed as Z sources (Hasinger & van der Klis 1989). These are further classified into Sco X-1 like and Cyg X-2 like sources based on the particular Z track traced by them (Kulkers *et al.* 1994, 1997). The various branches of this track are characterized by varying temporal and spectral features along them. The three main branches are the horizontal, normal and flaring branch (HB, NB and FB). The two existing contrary pictures to explain the motion of the source along the HID are the varying

mass accretion (\dot{m}) rate hypothesis (Hasinger *et al.* 1990; Vrtilik *et al.* 1990) and the constant mass accretion rate hypothesis where other physical or radial instabilities cause the source to trace out the Z-shaped track (Homan *et al.* 2002; Lin *et al.* 2012).

One of the fundamental characteristics of each branch is the signature of Quasi Periodic Oscillations (QPOs) exhibited in each of them (Hasinger & van der Klis 1989). QPOs in the horizontal branch (HB) termed as horizontal branch oscillations (HBOs) are found in the 15–60 Hz frequency range, while those in the normal branch (NB) termed as normal branch oscillations (NBOs) are found in the 5–8 Hz frequency range (van der Klis 2006). Flaring branch Oscillations, so far detected only in two sources Sco X-1 and GX 17+2 (Priedhorsky *et al.* 1986; Penninx *et al.* 1988; Homan *et al.* 2002), are found in the frequency range of 10–25 Hz. Each of these oscillations are considered to have different physical origins. Alpar and Shaham (1985) proposed a model where HBOs could be associated with

This article is part of the Special Issue on “AstroSat: Five Years in Orbit”.

the Keplerian orbital frequency of the inner edge of the disk and the spin frequency of the neutron star. Stella & Vietri (1999) and Stella *et al.* (1999) proposed the Relativistic Precession Model (RPM) that associates HBOs to the nodal precession of tilted orbits near the neutron star. NBOs and FBOs could possibly be oscillations in the optical depth of accretion flow in the inner disk region as proposed by Lamb *et al.* (1989) and Fortner *et al.* (1989) or they could be oscillations associated with the sound waves in a thick disk (Alpar & Shaham 1985). Another model for NBOs were proposed by Titarchuk *et al.* (2001), where these oscillations are considered to be acoustic oscillations of a spherical viscous shell around the NS.

Spectral modeling has been ambiguous in these sources, especially when it comes to the origin of soft and hard energy photons. As per the eastern spectral model, soft photons emanating from the disk are modeled using a multi-temperature black body emission (MCD, Mitsuda *et al.* 1984) and these photons are the seed for inverse Comptonization in the compact corona producing hard X-rays. The western model on the other hand uses a single temperature blackbody emission from the NS surface (or the immediate surrounding region) and a high energy power-law model for describing the hard emission (White *et al.* 1986). Another model proposed by Popham and Sunyaev (2001) considers a hot, low density boundary layer around the NS surface to be responsible for the hot Comptonized spectrum and the optically thick accretion disk to be responsible for the black body spectrum. Though both the models fairly describe the X-ray spectrum of Z sources, the picture is not clear in terms of understanding the location and size of corona and whether the accretion disk is truncated or not.

A vital timing tool to resolve some of these ambiguities in understanding the accretion disk corona geometry is a Cross Correlation Function (CCF) study between soft and hard X-ray energy bands (e.g. Vaughan *et al.* 1999; Sriram *et al.* 2007, 2012, 2019). Previous CCF studies of Z sources have led to the detection of lags of the order of hundred seconds in the HB and NB branch of the Z track while FBs are mostly seen to have strong positively correlated CCFs (Lei *et al.* 2008; Sriram *et al.* 2012, 2019). It was suggested that these lags are attributed to the readjustment of the coronal structure which could in effect help in constraining the size of the coronal structure (Sriram *et al.* 2019).

Here we present an extensive spectro-temporal study of the source GX 17+2 using the AstroSat LAXPC archival data of the source. GX 17+2 is a burster Z source with no confirmed optical counterparts, located at a distance of 13

kpc (Galloway *et al.* 2008), having a spin frequency of 293.2 Hz (Wijnands *et al.* 1997). GX 17+2 is a low inclination system $i < 40^\circ$ (Cackett *et al.* 2010; Ludlam *et al.* 2017; Malu *et al.* 2020). Cackett *et al.* (2010) used a relativistic diskline model on the Suzaku data of the source, which led to an estimate of 7–8 GM/c^2 for the inner disk radius. Using NuStar spectra of GX 17+2 (3–30 keV), Ludlam *et al.* (2017) determined that the disk extends to 1.0–1.02 ISCO. Sriram *et al.* (2019) based on the RXTE spectrum of the source estimated an inner disk radius of 20–35 km. Using the AstroSat spectrum of the source, Agrawal *et al.* (2020) found a decreasing power-law component along the Z track from HB to NB and this component was found to be increasing from the NB to FB. They estimated a 28–42 km inner disk radius from their spectral analysis. Based on the AstroSat SXT+LAXPC spectra, Malu *et al.* (2020) found an inner disk radii ~ 12 –16 km (5.7 – $8.0 R_g$), along the NB, which is close to ISCO. Hence the inner disk can be considered to be almost at the last stable orbit without much change in the position of the disk front.

Energy-dependent CCF studies of GX 17+2 using RXTE and NuStar data (3–5 keV and 16–30 keV) performed by Sriram *et al.* (2019) led to the detection of a few hundred second delays when the source was in the NB and HB. Using these lags the coronal height was constrained to be around 20–35 km. A similar study using the SXT (0.8–2 keV) and LAXPC (3–5 keV, 16–20 keV, 20–40 keV and 20–50 keV) data performed by Malu *et al.* (2020) again revealed lags of the order few hundred seconds in the NB of the Z track and the height of the corona was constrained to few tens of km. Here the spectral analysis revealed only a varying power-law index across the NB thus leading to the conclusion that only the hot Comptonized region was varying.

Earlier CCF study of GX 17+2 using AstroSat (Malu *et al.* 2020) was focused only on the NB and an extensive CCF study along with a correlated spectral and timing study of the source across the complete HID can help in resolving the inconsistencies related to the accretion disk corona geometry. Hence we report here, the CCF, PDS and spectral study of the source GX 17+2 using AstroSat's LAXPC data.

2. Data reduction and analysis

AstroSat Large Area X-ray Proportional Counter (LAXPC) archival data of the source was used in this study. Datasets used for the study include the Obs. ID

Table 1. CCF information of LAXPC soft (3–5 keV) vs. hard (16–40 keV) lightcurves. Here CC means cross-correlation coefficient. Lags refer to the CCF lags obtained and HID location gives the position of the lightcurve segment on the HID.

ObsID	Start time (UT)	Stop time (UT)	Exposure time (s)	CC ± CC _{err}	Lags ± error (s)	HID location (hard color, intensity)	χ ² /dof
G05-112T01-9000000452	2016-05-11, 12:27:21	2016-05-14, 11:17:27	2400	-0.37 ± 0.05	422 ± 85	550–600, 0.81–0.73	31/40
Section A ^a			3000	-0.55 ± 0.02	369 ± 30	540–580, 0.77–0.66	72/54
Section B			2900	-0.57 ± 0.03	306 ± 70	520–550, 0.75–0.67	27/37
Section C			3100	0.46 ± 0.03	-571 ± 37	460–500, 0.68–0.59	24/47
Section D			1700	-0.38 ± 0.05	555 ± 43	400–450, 0.62–0.54	25/32
Section E			3100	0.56 ± 0.02	-281 ± 31	470–520, 0.58–0.62	29/50
G08-037T01-90000002256	2018-07-26, 08:54:03	2018-07-26, 18:56:51	2300	-0.37 ± 0.04	-6 ± 36	540–570, 0.63–0.72	29/50
Section F			2700	-0.4 ± 0.04	-78 ± 55	530–560, 0.62–0.68	32/50
Section G	2018-09-10, 04:24:32	2018-09-10, 23:55:00	3200	-0.59 ± 0.03	-9 ± 26	520–550, 0.60–0.65	36/51
Section H			3600	-0.27 ± 0.03	604 ± 63	500–540, 0.58–0.64	25/31
Section I							
Section J							

^aDetected HBO.

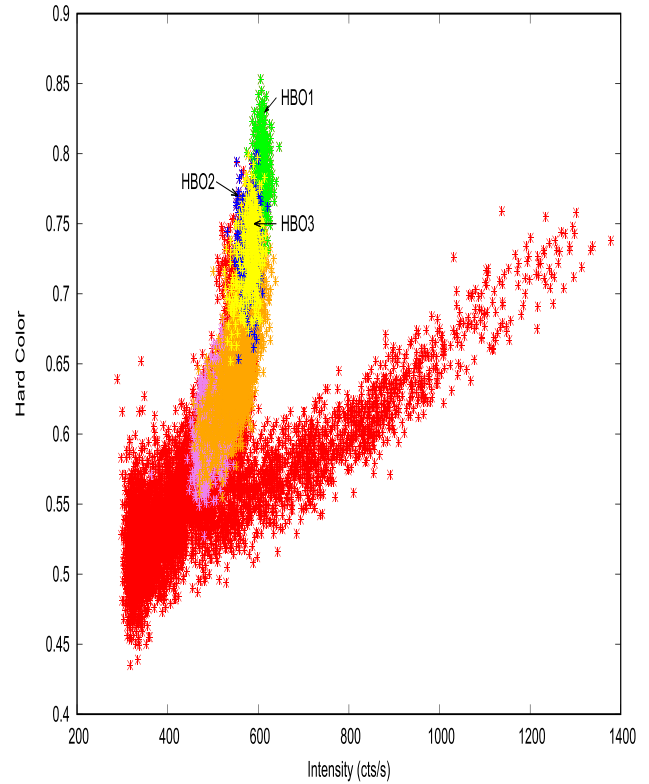


Figure 1. HID for GX 17+2 using AstroSat LAXPC observations. LAXPC 20 data was used. Hard colour is defined as 10.5–19.7/7.3–10.5 keV and Intensity is that in the 7.3–19.7 keV range. G05-112T01-9000000452 is represented using colours red, blue, green and yellow, T02-087T01-9000002352 is represented using colours orange. G08-037T01-9000002256 is represented using colour violet.

G05-112T01-9000000452 observed from 2016, May 11 to 2016, May 14 (~ 100 ks), Obs. ID T02-087T01-9000002352 observed on 2018, September 10 (~ 49 ks) and Obs. ID G08-037T01-9000002256 observed on July 26, 2018 (~ 18 ks).

LAXPC data in the EA mode was used for this study and this has a time resolution of 10 μs. LAXPC onboard AstroSat has three proportional counter units that are co-aligned – LAXPC 10, 20 and 30. The combined effective area is 6000 cm² at 15 keV and it is operational in the 3–80 keV energy range with a moderate energy resolution (Yadav *et al.* 2016; Antia *et al.* 2017).

The Level 1 data was analysed using LAXPC software (Format A May 19, 2018) which is provided by the AstroSat Science Support Center (ASSC). LAXPC_MAKE_EVENT, LAXPC_MAKE_STDGTI, LAXPC_MAKE_LIGHTCURVE and LAXPC_MAKE_SPECTRA modules were used to generate the event file, GTI file, corresponding lightcurves and

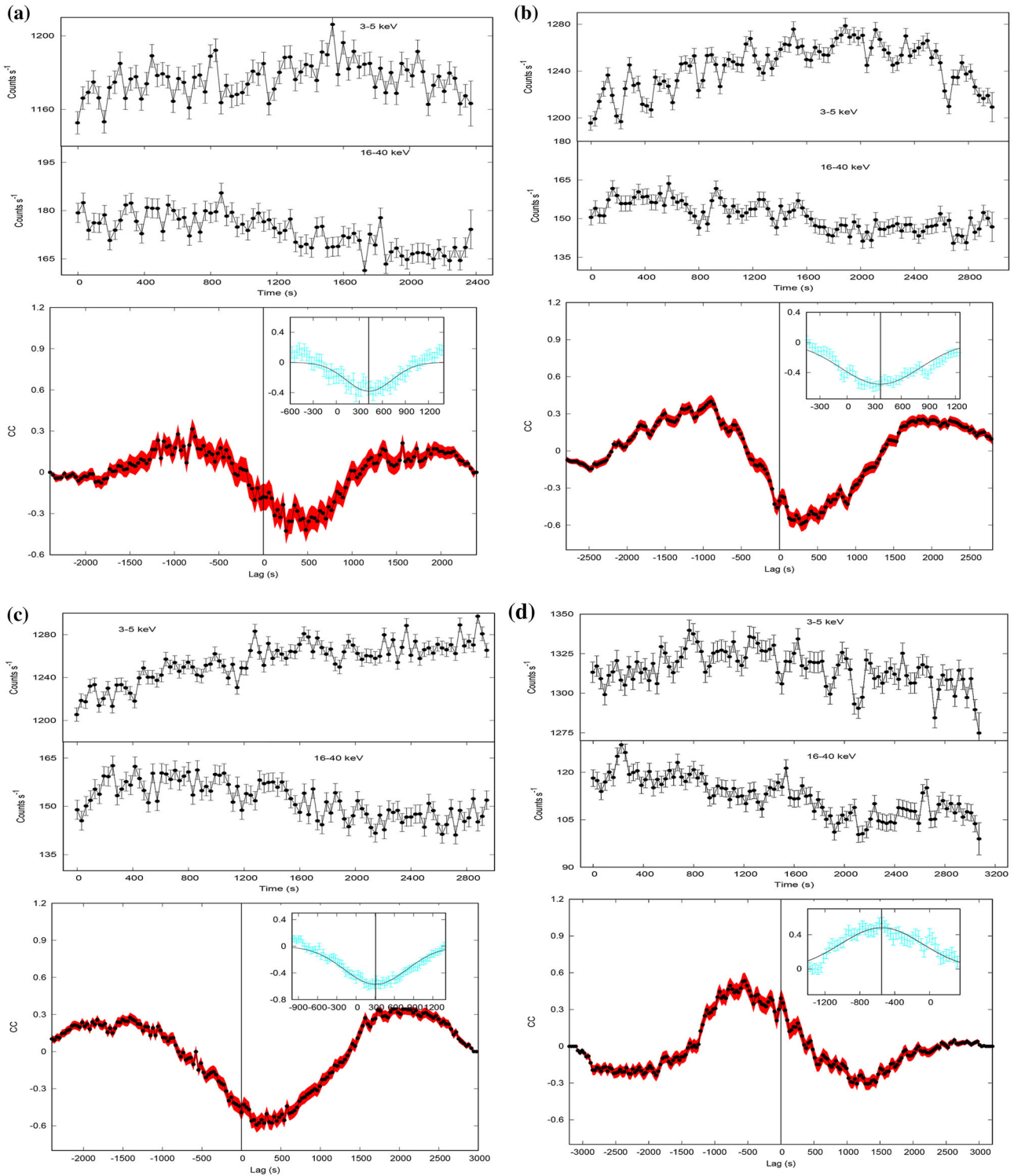


Figure 2. The background subtracted LAXPC soft (3–5 keV) and hard (16–40 keV) light curves on the top panels and the corresponding CCF lag observed are on the bottom panels. Energy bands used are mentioned in the light curves (top panel). Bottom panels show the cross correlation function (CCF) of each section of the light curve and shaded regions show the standard deviation of the CCFs. Bottom panel inset figure gives the Gaussian fit of the lag portion.

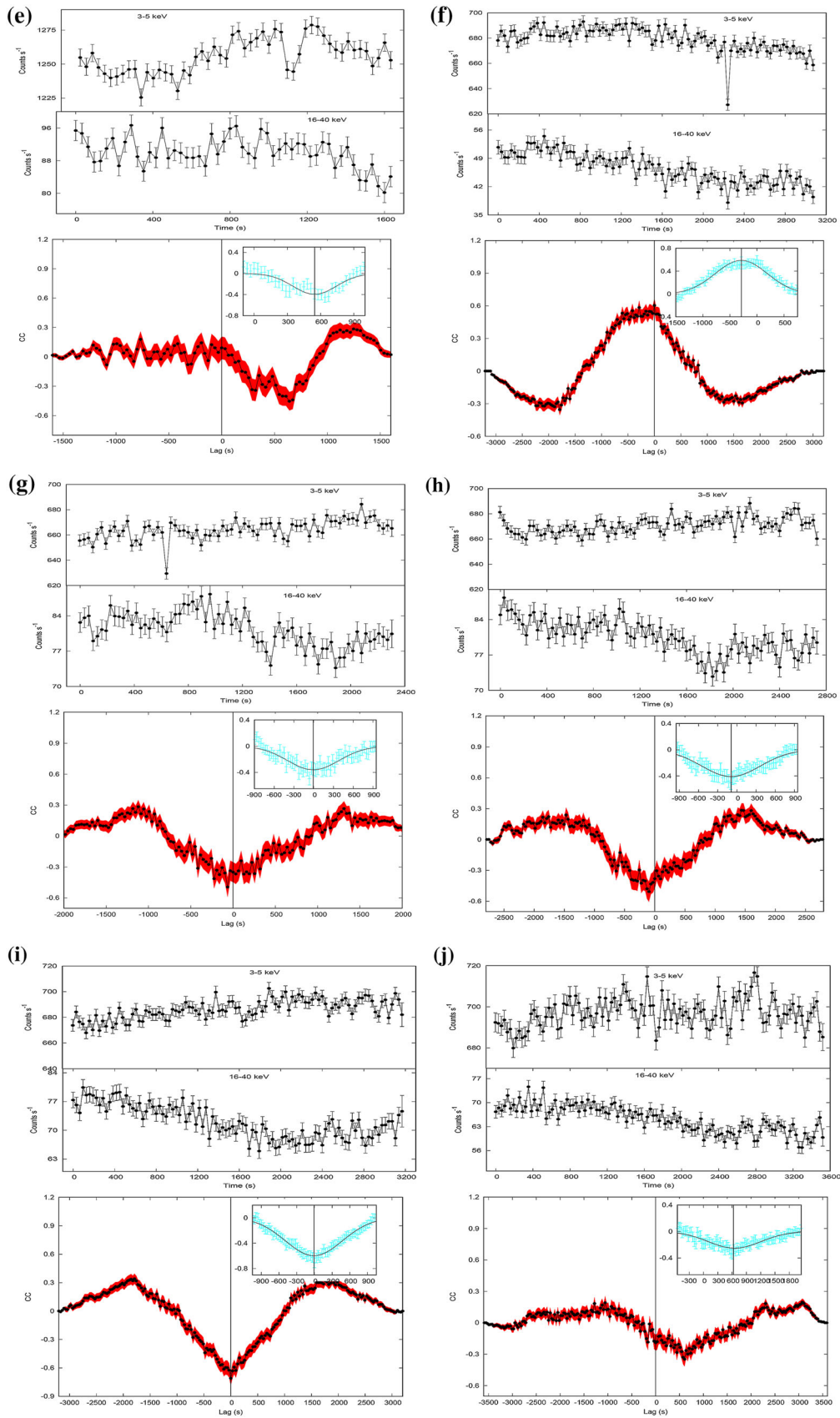


Figure 2. Continued.

spectra respectively. LAXPC_MAKE_BACKLIGHT CURVE and LAXPC_MAKE_BACKSPECTRUM were used to generate the corresponding background light curves and spectrum. The corresponding response files were generated along with it. Spectrum in the 3–50 keV band was used for the study and 1% systematic error was considered (Agrawal *et al.* 2020). LAXPC10 data has been used for spectral analysis (otherwise mentioned) as it is better calibrated and have less background issues when compared to other LAXPC units. LAXPC 20 data has been used for timing analysis for observations during 2018, due to low gain operation of LAXPC 10. For remaining observations LAXPC 10 and 20 has been used.

3. Timing analysis

Timing analysis was performed on the background subtracted binned LAXPC10 and LAXPC20 light curves of GX 17+2. Using the hard colour 10.5–19.7 keV/7.3–10.5 keV and intensity in the range 7.3–19.7 keV, the HID was obtained for sections that exhibited CCF lags (see Table 1). The light curves were corrected for dead-time effects (van der Klis 1988); for LAXPC the dead time is 42.5 μ s (Yadav *et al.* 2016). For all the datasets, LAXPC 20 data was used to obtain the HID (Fig. 1).

Crosscor tool of XRONOS package was used to perform the cross correlation function (CCF) analysis (Sriram *et al.* 2007; Lei *et al.* 2008). We used the direct slow method (fast = no) to compute the correlation coefficients (CC) as a function of lags between the two light curves. The error bars of CCF are obtained by propagating the theoretical error bars of the cross correlations from the individual intervals and the cross correlations are normalized by dividing them with the square root of the product of newbins of the two light curves in each interval.¹ CCF analysis was performed between the 3–5 keV (soft) and 16–40 keV (hard) 32 s binned light curves (Sriram *et al.* 2007, 2012, 2019; Lei *et al.* 2008; Malu *et al.* 2020). The top panel of Fig. 2 shows the soft and hard energy band light curves of each section and the bottom panel shows the CCF along with the Gaussian fit (inset) of each section where lag was observed. In order to estimate the CCF lags, we adopted a procedure wherein several different segments were considered

around the hypothetical centroid and Gaussian functions were fitted. The minimum χ^2 fit was considered to estimate the CCF lags and their errors were estimated with a 90% confidence level using the criterion of $\Delta\chi^2 = 2.71$ (see Table 1). Figure 3 shows few of the representative lag vs. $\Delta\chi^2 (= \chi^2 - \chi_{\min}^2)$ figures obtained from the above mentioned procedure.

In the Obs. ID G05-112T01-9000000452, lags were found in five different light curve segments. CCF lags varying from ~ 306 –571 s were found in HB and NB with a correlation coefficients (CC) varying from ~ 0.4 –0.6 for the lags (see Table 1). This is consistent with that obtained from previous studies (Sriram *et al.* 2019). Out of the five segments, one was a positively correlated soft lag and remaining were anti-correlated hard lags. For Obs. ID G08-037T01-9000002256, lag was found in one section with a lag of 281 ± 31 s (CC = 0.58 ± 0.03 , positively correlated soft lag) in the HB. For Obs. ID T02-087T01-9000002352, again four segments were found to exhibit lags in the HB varying from 78–604 s, with four of them showing anti-correlated lags. One segment was associated with hard lags (see Table 1 and Fig. 2). Two of the sections (G and I) show anticorrelated CCFs but with almost no significant lags.

Power Density Spectrum (PDS) was obtained using a 1/2048 s binned light curves in the 3–20 keV energy band, using LAXPC10 and LAXPC20 in order to improve the statistics. According to the normalization method by Miyamoto *et al.* (1991), power density spectra (PDS) were normalized in units of (rms/mean)²/Hz. PDS were fitted with a one or two Lorentzian and power-law model (see Table 2). PDS has revealed a ~ 25 Hz and ~ 33 Hz HBO in the G05-112T01-9000000452 (orbit 03352, 03353, 03355), when the source was in the HB (see Table 2). For one of the light curve segments (orbit 03352), PDS revealed a 25.04 ± 0.44 Hz HBO with a 50.37 ± 0.43 Hz harmonic. For orbit 03353, a 32.34 ± 0.23 Hz HBO with a harmonic of 61.74 ± 4.75 Hz was observed. This section also exhibits an anti-correlated hard lag of 426 ± 38 s. Another segment (orbit 03355) revealed a 35.24 ± 0.33 Hz HBO with no harmonic (see Fig. 4 and Table 2).

4. Spectral analysis

In order to check if any associated spectral variations are present, spectral analysis was performed for the first and last 1000 s of light curve segments (marked (a), (b) in Table 3, Fig. 2) which exhibited significant

¹<https://heasarc.gsfc.nasa.gov/docs/xandau/xronos/help/crosscor.html>.

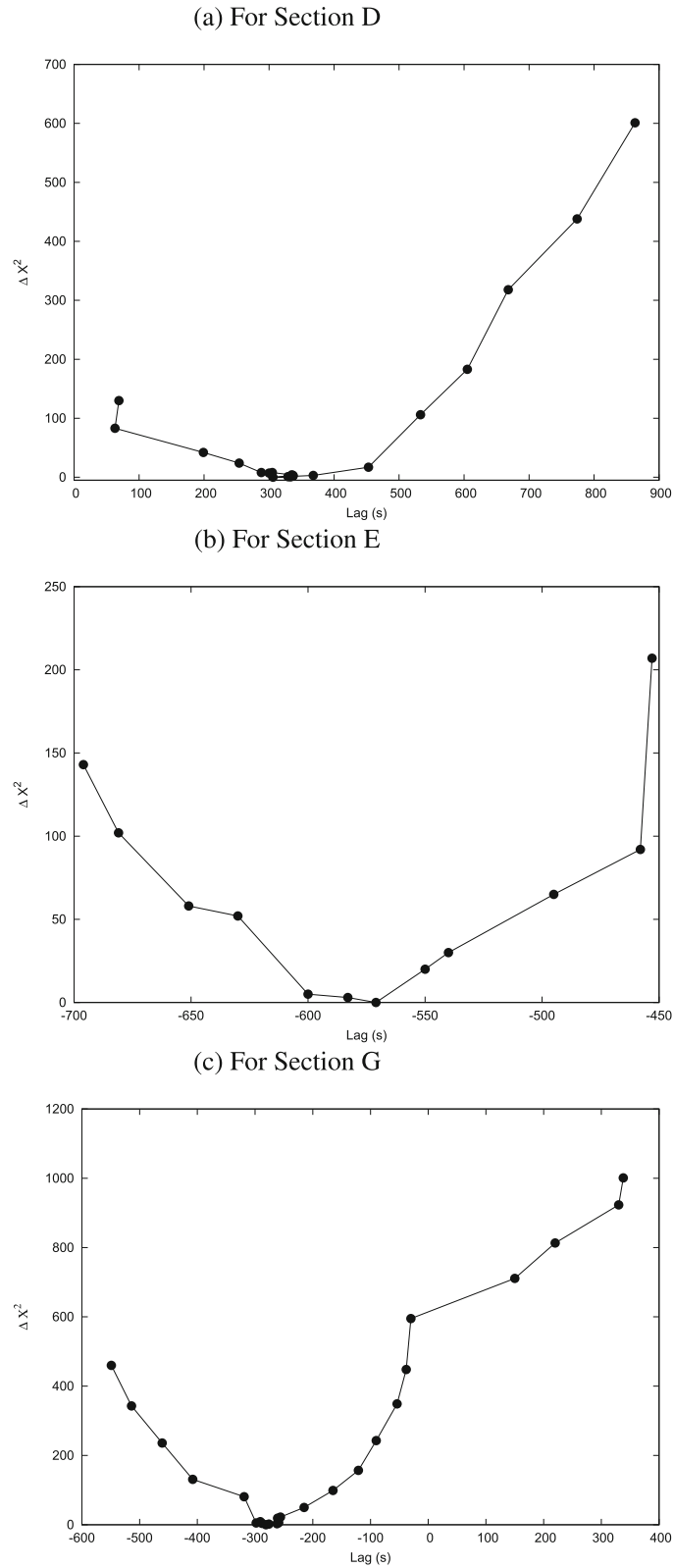


Figure 3. The CCF lag vs. $\Delta\chi^2$ ($= \chi^2 - \chi^2_{\min}$) plot obtained from the procedure mentioned in Section 3.

lags and separately for those segments which exhibited HBOs (Table 4, Fig. 4). Spectra were fitted in the 3–50 keV energy range using XSPEC v12.10.1f

(Arnaud 1996) and uncertainties were estimated with a 90% confidence level ($\Delta\chi^2 = 2.71$). Figures 5, 6, 7 and 8 show the top panel with the unfolded spectra

Table 2. HBO parameter values.

Observation Id: G05-112T01-9000000452			
Orbit	HBO ν (Hz)	$\Delta\nu$ (Hz)	RMS %
03352	25.04±0.44	5.97±1.91	1.21±0.11
	50.37±0.43	5.67±2.75	1.60±0.14
03353	32.34±0.23	1.77±0.28	0.96±0.08
	61.74±4.75	13.74±6.13	1.53±0.14
03355	35.24±0.33	4.41±1.18	1.06±0.10

(thick line) along with the model components (dashed line) and the bottom panel with the residuals to the fit. Absorption column density was modeled using the *Tbabs* model (Wilms *et al.* 2000) and was fixed at $\sim 2.2 \times 10^{22} \text{ cm}^{-2}$ (Cackett *et al.* 2010). Using the continuum model *DiskBB* + *bbody* + *power-law* (Cackett *et al.* 2008, 2010; Lin *et al.* 2007), the spectra were fitted which led to residuals around 6.7 keV which was then modeled using a Gaussian function centered at 6.7 keV (fixed) resulting in lower reduced χ^2/dof values (see Table 3, Fig. 4). Gaussian and power-law component models are needed to unfold the spectra as indicated by the values of F-test probability (Table 3). χ^2/dof values before adding the power-law component was noted to be 93.69/39, 112.21/39 for Section A(a), (b) which is significantly higher compared to that obtained after incorporating the power-law component, i.e. 29.72/37, 47.54/37. Spectral parameters are found to be non-varying (within error bars) for the first and last 1000 s sections of each segment that exhibited lags (see Table 3). During these observations, the inner disk temperature (kT_{in}) was different, ranging from 1.66–2.02 keV. It should be noted that kT_{in} and kT_{BB} are affected by the spectral hardening factor (f_{col} ; for more details, see Davis *et al.* 2005).

The effective temperature is given by $T_{\text{eff}} = kT_{\text{in}}/f_{\text{col}}$ and T_{eff} was found to be in the range of 1.03–1.26 keV for $f_{\text{col}} = 1.6$ (Davis *et al.* 2005). We did not find any significant variation in the spectral parameters between the final and last sections of each observation. There is a slight change in total flux in B and D sections (Table 3). The spectral analysis of sections exhibiting HBOs (Table 5, Fig. 7) suggest that the disk is close to the last stable orbit during the HB and we did not find any significant variation in the spectral parameters when the source varied from ~ 25 Hz to ~ 33 Hz HBOs.

We have also unfolded the spectra of various sections using a thermal comptonization model viz.

NthComp + *Gaussian* + *power-law*) (Agrawal *et al.* 2020). In the *NthComp* model, soft seed photons are assumed to be a black body emission (Zdziarski *et al.* 1996). Based on the F-test probability in all the sections, we find that the power-law model is necessary for the data (Tables 4 and 6). Unfolded spectra for various sections are shown in Figures 6 and 8. For the fits, we fixed the power-law index, Γ at 3.0 in order to constrain the other parameters. The reason to fix Γ came from the study of Agrawal *et al.* (2020), as in most of the branches, spectra exhibit Γ around 3. We noted that even if we vary Γ from 2.9 to 3.1, there is no noticeable variation in other spectral parameters. We found that for e.g. Section A, Γ_{NthComp} varied slightly from 1.80 to 1.94 with in 90% confidence level. Similar small changes were observed in kT_e for Sections A and D. Total fluxes were found to be slightly varying in subsections i.e. (a) and (b) of Sections B and D (Table 4).

5. Results and discussion

5.1 Constraining the inner disk radius

Based on the PDS analysis, we found HBOs with a centroid frequency ~ 25 Hz and 33 Hz. Based on the relativistic precession model (RPM), higher frequency kHz QPOs, lower frequency kHz QPOs and HBOs correspond to the Keplerian, periastron precession and nodal precession frequencies, respectively (Stella & Vietri 1999; Stella *et al.* 1999).

Based on the equation given by Di Matteo and Psaltis *et al.* (1999), we can estimate an upper limit to the inner disk radius. It should be noted that the below relation is based on the empirical correlation between HBOs and the upper kHz QPO $\nu_{\text{HBO}} = 63 \times (\nu_{\text{upp}}/1 \text{ kHz})^{1.9}$ reported by Psaltis *et al.* (1999). This relation should be verified for GX 17+2 by considering all the available detections of QPOs.

$$\frac{R_{\text{in}}}{R_g} \leq 27\nu^{-0.35} \left[\frac{M}{2M_{\odot}} \right]^{-2/3} \quad (1)$$

With $\nu = 25$ Hz, we found R_{in} to be ~ 23 km and with $\nu = 33$ Hz, we found R_{in} to be ~ 21 km.

5.2 Constraining the inner disk radius: TL model

We constrained the inner disk radius using the transition layer (TL) model (Titarchuk & Osherovich

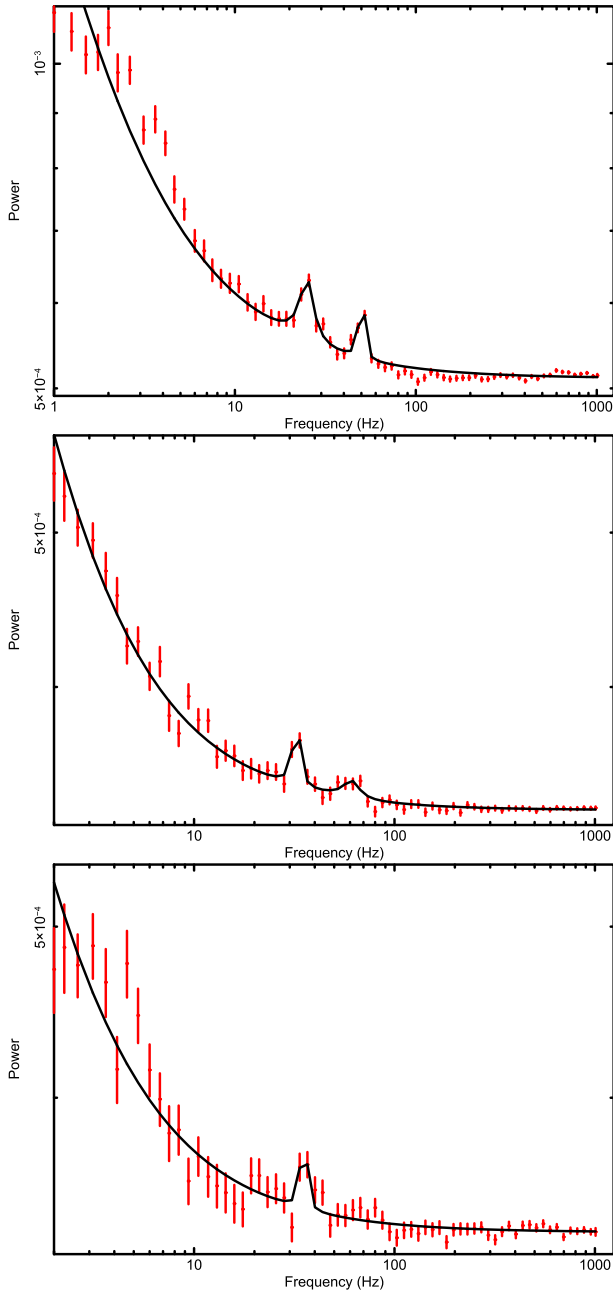


Figure 4. HBOs seen in Observation Id G05-112T01-9000000452 for the light curve in 3–20 keV energy range using AstroSat LAXPC observations fitted using a Lorentzian and powerlaw model to the PDS.

1999; Osherovich & Titarchuk 1999a, b). Using the correlation equation between HBO and kHz QPO in Z sources given by Wu (2001) and the relation between kHz QPO and inner disk radius given by Matteo and Psaltis (1999), Sriram *et al.* (2009) arrived at an equation connecting HBO frequency and the inner disk radius as below:

$$\frac{R_{\text{in}}}{R_g} = 220 \left[\left(\frac{\Omega}{\pi} \right)^{-2/3} \left(\left(\frac{\Omega \sin \delta}{v_{\text{HBO}} \pi} \right)^2 - 1 \right)^{1/3} \right] \left[\frac{M}{10M_{\odot}} \right]^{-2/3}, \quad (2)$$

where δ is the angle between rotational angular velocity (Ω) and normal to the Keplerian oscillation ($\delta = 6.30$ for GX 17+2; Wu 2001).

We found R_{in} to be $\sim 21R_g$ (~ 44 km; $R_g = GM/c^2$) for 25 Hz HBO.

For $\nu \sim 25$ Hz, we found R_{in} to be $\sim 22R_g$ (~ 46 km) and for $\nu \sim 33$ Hz, $R_{\text{in}} \sim 18R_g \sim 38$ km).

5.3 Inner disk radii from spectral modeling

Based on the DiskBB model normalization (Mitsuda *et al.* 1984), N_{dBB} is proportional to the inner disk radius. Using the equation, R_{in} (km) = $\sqrt{(N/\cos i)} \times D/10$ kpc, and taking $i = 28^\circ$ (Malu *et al.* 2020), we estimated the inner disk radii R_{in} to be 9.79 km (A(a)), 7.91 km (A(b)), 8.78 km (B(a)), 10.59 km (B(b)), 11.68 km (C(a)), 11.02 km (C(b)), 13.12 km (D(a)), 11.75 km (D(b)).

Since these radii needs to be corrected for spectral hardening using the relation, $R_{\text{eff}} = \kappa^2 \xi R_{\text{in}}$ (Kubota *et al.* 2001) where $\kappa \sim 1.7$ – 2.0 (Shimura & Takahara 1995) and $\xi = 0.41$ (Kubota *et al.* 1998), we estimate the R_{in} to be 11.55–16.06 km (A(a)), 9.34–12.97 km (A(b)), 10.37–14.41 km (B(a)), 12.49–17.36 km (B(b)), 13.79–19.16 km (C(a)), 13.01–18.08 km (C(b)), 15.49–21.52 km (D(a)) and 13.87–19.27 km (D(b)), which is close to that estimated by Cackett *et al.* (2009), Ludlam *et al.* (2017), Agrawal *et al.* (2020) and Malu *et al.* (2020) and for GX 17+2. The derived R_{in} values suggest that disk front is found to be near or almost at the last stable orbit. Along the HID track we find no change in the inner radius, hence suggesting that it could be the coronal structure which is responsible for the source traversing along the HID and not the mass accretion rate. This is similar to the results by Lin *et al.* (2012) and Homan *et al.* (2002).

5.4 Coronal height estimation from CCF lags

An extensive timing and spectral study using the archival data of AstroSat LAXPC for GX 17+2 is reported here. Based on the CCF study between LAXPC soft (3–5 keV) and hard (16–40 keV) light

Table 3. Best-fit spectral parameters for sections which exhibited lags using DiskBB + Gaussian + bbody + Power-law model. The subscript BB represents the bbody model and dBB represents DiskBB model. The flux in units of 10^{-8} ergs cm^{-2} s^{-1} is calculated in the energy band 3–50 keV. Errors are quoted at a 90% confidence level. Luminosity is in units of 10^{38} erg s^{-1} assuming the distance 13 kpc for GX 17+2. Mass accretion rate is in units of 10^{18} g s^{-1} .

Parameter	A		B		C		D	
	(a)	(b)	(a)	(b)	(a)	(b)	(a)	(b)
kT_{in} (keV) ^a	1.74±0.16	2.02±0.15	1.87±0.18	1.78±0.13	1.66±0.15	1.74±0.15	1.66 ± 0.12	1.80 ± 0.09
$N_{\text{dBB}}^{\text{b}}$	50.10±23.2	32.71±9.42	40.32±16.12	58.56±19.6	71.34±31.12	63.51±24.31	90.04 ± 33.12	72.15 ± 15.23
R_{in} ($i = 28^\circ$) ^c	9.79 km	7.91 km	8.78 km	10.59 km	11.68 km	11.02 km	13.12 km	11.75 km
R_{eff} ($i = 28^\circ$) ^d	11.55–16.06 km	9.34–12.97 km	10.37–14.41 km	12.49–17.36 km	13.79–19.16 km	13.01–18.08 km	15.49–21.52 km	13.87–19.27 km
kT_{BB} (keV) ^e	2.84±0.07	3.04±0.10	2.84±0.10	2.80±0.08	2.68±0.07	2.73±0.08	2.60 ± 0.07	2.79 ± 0.08
N_{BB}^{f}	0.083±0.006	0.074±0.006	0.069±0.007	0.075±0.006	0.080±0.007	0.075±0.007	0.072±0.007	0.063±0.005
$\Gamma_{\text{pl}}^{\text{g}}$	2.93±0.11	3.42±0.22	3.01±0.10	3.11±0.14	2.89±0.12	2.98±0.13	2.88±0.21	3.24±0.20
N_{pl}^{h}	6.80±2.17	12.02±3.81	7.65±2.17	7.01±2.62	6.07±2.36	6.20±2.40	3.96±2.47	3.06±1.95
E_{Fe} (keV) ⁱ	6.7	6.7	6.7	6.7	6.7	6.7	6.7	6.7
σ_{Fe} (keV) ^j	0.91±0.40	0.86±0.48	0.56±0.53	0.75±0.47	0.84±0.45	0.84±0.52	0.78±0.63	0.78±0.54
N_{Fe}^{k}	0.021±0.011	0.015±0.008	0.014±0.008	0.016±0.008	0.020±0.011	0.018±0.010	0.017±0.011	0.014±0.009
DiskBB flux	0.50±0.06	0.66±0.09	0.56±0.08	0.65±0.06	0.55±0.06	0.63±0.07	0.70±0.07	0.83±0.11
bbody flux	0.66±0.06	0.59±0.07	0.55±0.06	0.60±0.06	0.64±0.05	0.59±0.06	0.57±0.01	0.50±0.04
Powerlaw flux	0.36±0.06	0.25±0.06	0.36±0.03	0.26±0.05	0.35±0.06	0.30±0.07	0.23±0.08	0.26±0.04
Total flux	1.55±0.01	1.53±0.02	1.48±0.01	1.53±0.01	1.57±0.01	1.55±0.01	1.52±0.01	1.46±0.01
L_{3-50}	3.12 ± 0.02	3.08 ± 0.04	2.98±0.02	3.08 ± 0.02	3.16±0.02	3.12 ± 0.02	3.06±0.02	2.94±0.02
\dot{m}	1.67 ± 0.01	1.65±0.02	1.60±0.01	1.65 ± 0.01	1.69±0.01	1.67±0.01	1.64±0.01	1.57±0.01
χ^2/dof	29.72/37	47.54/37	28.31/37	31.96/37	38.02/37	34.98/37	30.31/37	32.98/37
χ^2/dof (without power-law)	93.69/39	112.21/39	76.06/39	67.96/39	87.22/39	211.60/39	70.30/39	64.97/39
Lag observed	422 ± 85 s			369 ± 30 s				–571±37 s
H_{e}^{l}	98–489 km			78–392 km				104–519 km
F-test (Gaussian prob.)	1.39×10^{-6}	1.37×10^{-3}	1.02×10^{-5}	2.16×10^{-5}	1.57×10^{-5}	4.346×10^{-5}	1.28×10^{-6}	2.17×10^{-3}
F-test (powerlaw prob.)	5.95×10^{-10}	1.25×10^{-7}	1.14×10^{-8}	8.68×10^{-7}	2.13×10^{-7}	3.45×10^{-15}	1.74×10^{-7}	3.56×10^{-6}

^aTemperature of the DiskBB model. ^bNormalization of the DiskBB model. ^cInner disk radii from DiskBB normalization. ^dEffective radius obtained by using DiskBB normalization and the spectral corrections 1.18–1.64. ^eTemperature of the BB model. ^fNormalization of the BB model. ^gPower-law index. ^hNormalization of the PL model. ⁱLine energy of the Gaussian model for iron line. ^jLine width of the Gaussian model for iron line. ^kNormalization of the Gaussian model for iron line. ^lCoronal height estimated from lag.

Table 4. Best-fit spectral parameters for sections exhibiting lags using NthComp + Gaussian + Power-law model. The flux in units of 10^{-8} ergs cm^{-2} s^{-1} is calculated in the energy band 3–50 keV. Errors are quoted at a 90% confidence level. Luminosity is in units of 10^{38} erg s^{-1} , assuming the distance 13 kpc for GX 17+2. Mass accretion rate is in units of 10^{18} g s^{-1} .

Parameter	A		B		C		D	
	(a)	(b)	(a)	(b)	(a)	(b)	(a)	(b)
Γ_{pl}^a	3.0	3.0	3.0	3.0	3.0	3.0	3.0	3.0
$N_{pl}6^b$	7.27 ± 1.02	6.52 ± 0.95	6.45 ± 1.02	3.42 ± 0.99	7.73 ± 0.90	5.59 ± 0.91	5.20 ± 0.77	5.36 ± 0.86
E_{Fe} (keV) ^c	6.7	6.7	6.7	6.7	6.7	6.7	6.7	6.7
σ_{Fe} (keV) ^d	0.77 ± 0.30	0.95 ± 0.29	0.80 ± 0.32	0.76 ± 0.29	0.67 ± 0.31	0.81 ± 0.35	0.74 ± 0.37	0.97 ± 0.21
N_{Fe}^e	0.019 ± 0.007	0.022 ± 0.006	0.018 ± 0.007	0.019 ± 0.006	0.018 ± 0.007	0.20 ± 0.007	0.019 ± 0.008	0.027 ± 0.006
$\Gamma_{NthComp}^f$	1.80 ± 0.04	1.94 ± 0.04	1.88 ± 0.04	1.98 ± 0.03	1.87 ± 0.04	1.95 ± 0.04	2.04 ± 0.04	2.15 ± 0.02
kT_e (keV) ^g	3.22 ± 0.07	3.45 ± 0.07	3.19 ± 0.08	3.25 ± 0.07	3.07 ± 0.07	3.13 ± 0.07	2.98 ± 0.07	3.21 ± 0.04
kT_{bb} (keV) ^h	0.64 ± 0.09	0.42 ± 0.07	0.66 ± 0.08	0.60 ± 0.06	0.69 ± 0.07	0.66 ± 0.06	0.70 ± 0.05	0.59 ± 0.04
$N_{NthComp}^i$	0.64 ± 0.12	0.72 ± 0.18	0.68 ± 0.16	1.09 ± 0.22	0.64 ± 0.13	0.82 ± 0.15	0.82 ± 0.12	0.92 ± 0.22
NthComp flux	1.19 ± 0.05	1.17 ± 0.04	1.16 ± 0.04	1.35 ± 0.04	1.18 ± 0.04	1.27 ± 0.04	1.26 ± 0.03	1.21 ± 0.04
Powerlaw flux	0.34 ± 0.05	0.28 ± 0.05	0.30 ± 0.05	0.16 ± 0.05	0.36 ± 0.04	0.26 ± 0.04	0.24 ± 0.04	0.28 ± 0.05
Total flux	1.55 ± 0.01	1.52 ± 0.01	1.48 ± 0.01	1.53 ± 0.01	1.56 ± 0.01	1.55 ± 0.01	1.52 ± 0.01	1.46 ± 0.01
L_{3-50}	3.12 ± 0.02	3.06 ± 0.02	2.98 ± 0.02	3.08 ± 0.02	3.14 ± 0.02	3.12 ± 0.02	3.06 ± 0.02	2.94 ± 0.02
\dot{m}	1.67 ± 0.01	1.64 ± 0.01	1.60 ± 0.01	1.65 ± 0.01	1.68 ± 0.01	1.67 ± 0.01	1.64 ± 0.01	1.57 ± 0.01
χ^2/dof	35.64/38	44.47/38	26.18/38	30.04/38	42.52/38	34.40/38	35.67/38	31.50/38
χ^2/dof (without power-law)	139.46/39	48.04/39	107.35/39	57.43/39	188.0/39	114.27/39	131.06/39	101.30/39
F-test (Gaussian) prob.	9.91×10^{-7}	1.23×10^{-6}	1.79×10^{-7}	1.16×10^{-7}	1.17×10^{-5}	1.95×10^{-6}	3.67×10^{-6}	8.78×10^{-9}
F-test (powerlaw) prob.	8.16×10^{-13}	8.87×10^{-2}	3.33×10^{-13}	8.15×10^{-7}	7.87×10^{-14}	1.88×10^{-11}	2.72×10^{-12}	3.52×10^{-11}

^aPowerlaw index. ^bNormalization of the PL model. ^cLine energy of the Gaussian model for iron line. ^dLine width of the Gaussian model for iron line. ^eNormalization of the Gaussian model for iron line. ^fNthComp power-law index. ^gElectron temperature (NthComp). ^hSeed photon temperature (NthComp). ⁱNormalization of the NthComp model.

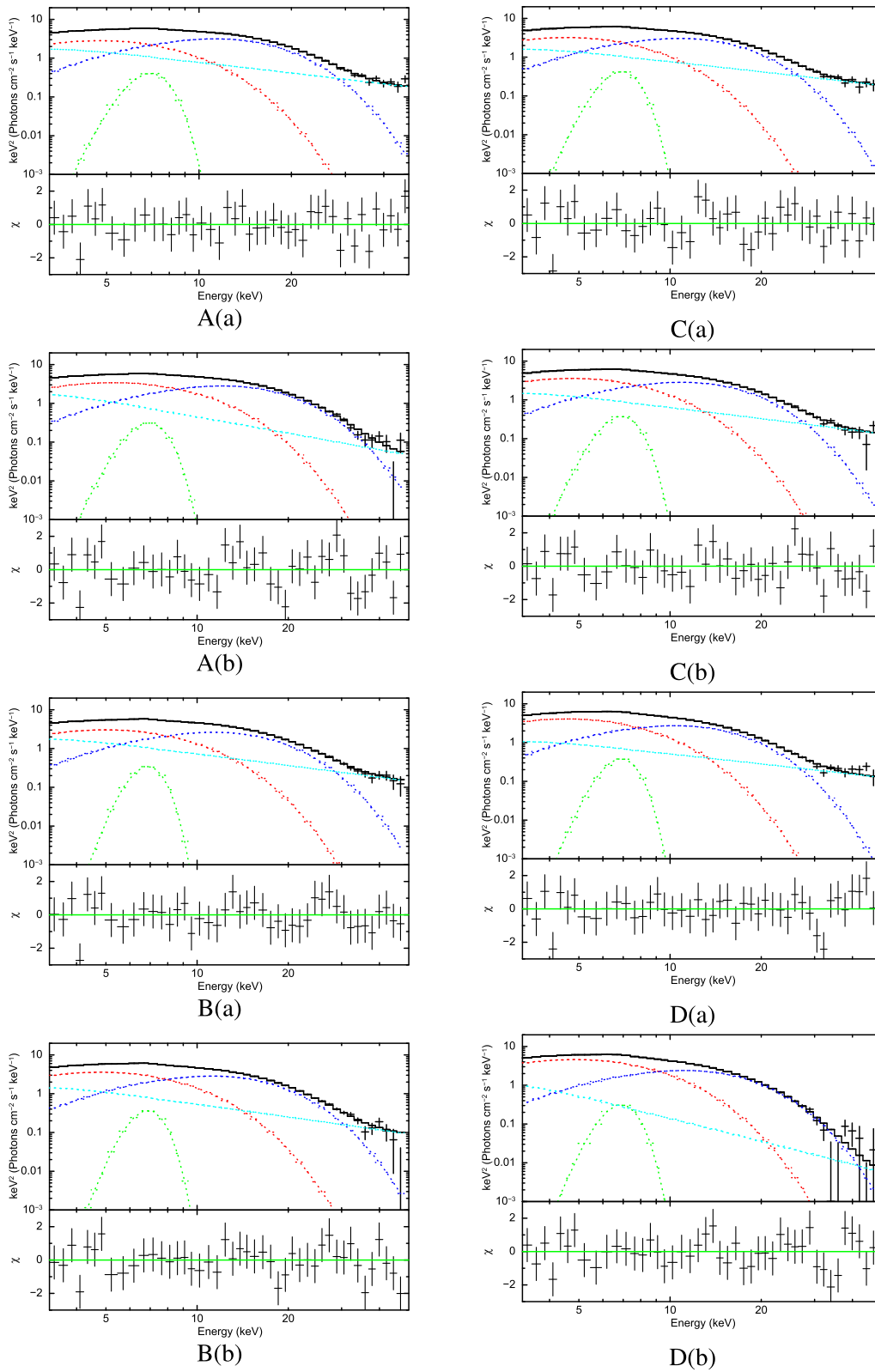


Figure 5. The LAXPC 10 spectral fit for the the *DiskBB* + *Gaussian* + *bbody* + *Powerlaw* model. The top panel gives the unfolded spectra (thick line) with the component models (dashed lines) and the bottom panel gives the residuals obtained from the fit. Here in the top panel, the light green colour line gives the Gaussian model component, cyan gives the Powerlaw component, red gives the diskBB component and dark blue gives the bbody component.

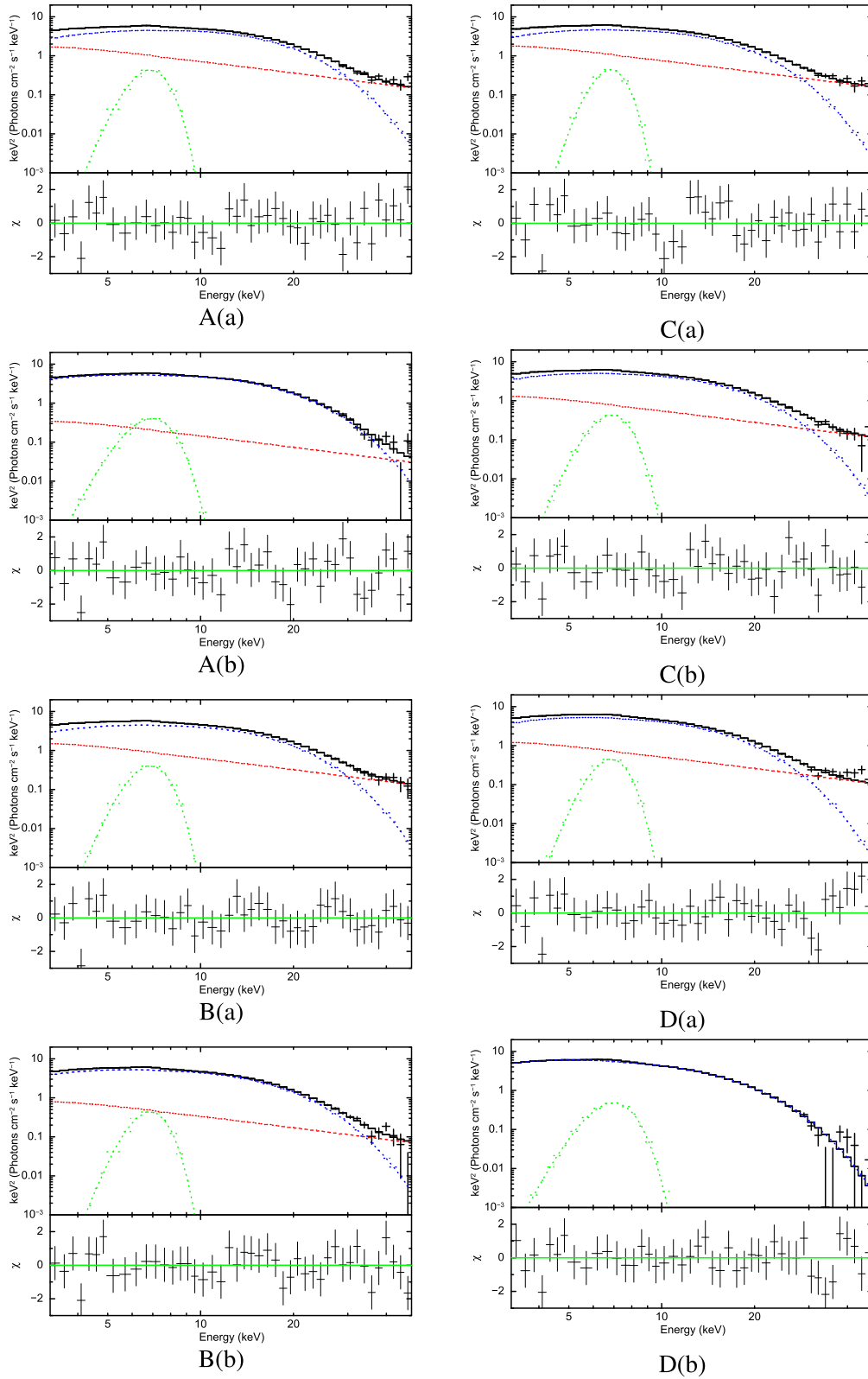
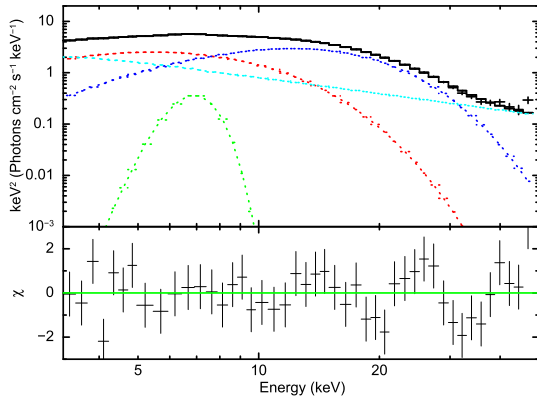
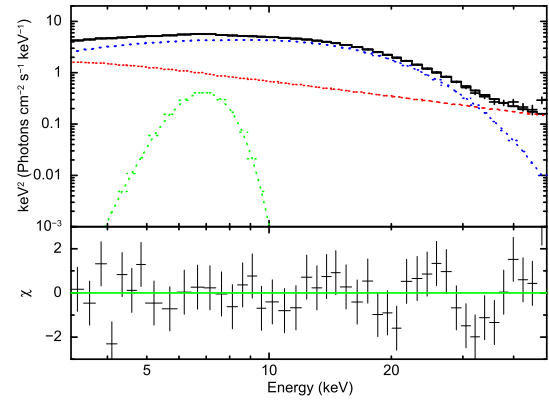


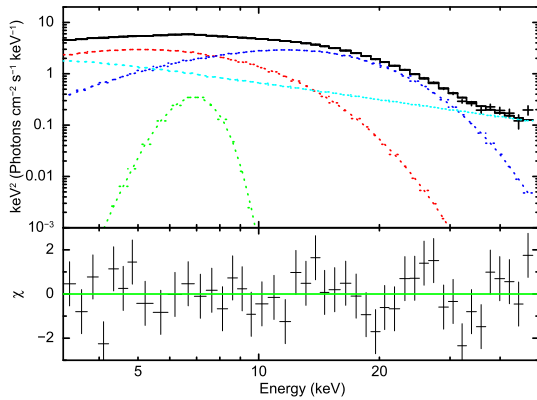
Figure 6. The LAXPC 10 spectral fit for the *NthComp* + *Gaussian* + *Power-law* model. The top panel gives the unfolded spectra (thick line) with the component models (dashed lines) and the bottom panel gives the residuals obtained from the fit. Here in the top panel, the light green colour line gives the Gaussian model component, red gives the Power-law component and dark blue gives the *NthComp* component.



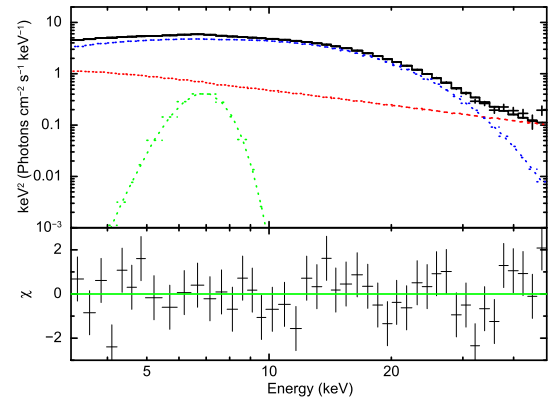
For HBO 1



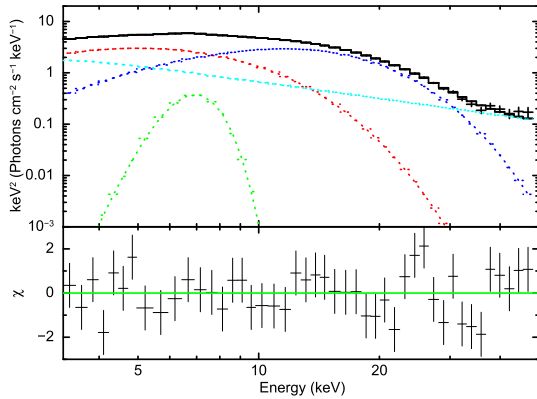
For HBO 1



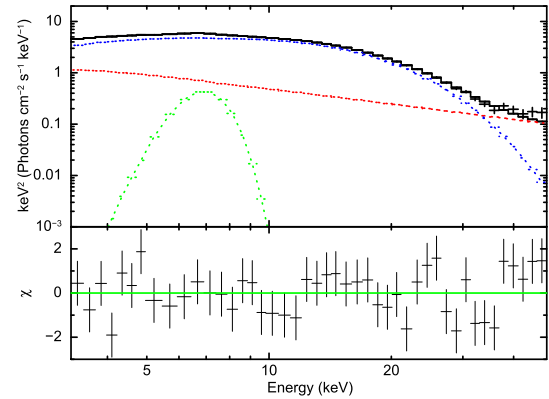
For HBO 2



For HBO 2



For HBO 3



For HBO 3

Figure 7. The LAXPC 10 spectral fit for the segments exhibiting HBOs using the *DiskBB + Gaussian + bbody + Powerlaw* model. The top panel gives the unfolded spectra (thick line) with the component models (dashed lines) and the bottom panel gives the residuals obtained from the fit. Here in the top panel, the light green colour line gives the Gaussian model component, cyan gives the power-law component, red gives the diskBB component and dark blue gives the bbody component.

Figure 8. The LAXPC 10 spectral fit for the segments exhibiting HBOs using the *NthComp + Gaussian + Powerlaw* model. The top panel gives the unfolded spectra (thick line) with the component models (dashed lines) and the bottom panel gives the residuals obtained from the fit. Here in the top panel, the light green colour line gives the Gaussian model component, red gives the Powerlaw component and dark blue gives the NthComp component.

curves, we detect correlated and anti-correlated lags of the order of few hundred seconds (see Table 1). This is in accordance with previously observed results for

this source (Sriram *et al.* 2019; Malu *et al.* 2020). The hard component could be arising from a coronal structure or a hot boundary layer component. Previous

Table 5. Best-fit spectral parameters for sections which exhibited HBOs using DiskBB + Gaussian + bbody + Power-law model. The subscript BB represents the bbody model and dBB represents DiskBB model. The flux in units of 10^{-8} ergs $\text{cm}^{-2} \text{s}^{-1}$ is calculated in the energy band 3–50 keV. Errors are quoted at a 90% confidence level. Luminosity is in units of 10^{38} erg s^{-1} assuming the distance 13 kpc for GX 17+2. Mass accretion rate is in units of 10^{18} g s^{-1} .

Parameter	For HBO 1	For HBO 2	For HBO 3
kT_{in} (keV) ^a	2.10±0.21	1.92±0.14	1.87±0.13
N_{dBB} ^b	20.53±7.89	33.52±11.32	39.54±12.75
R_{eff} ($i = 28^\circ$) ^c	7.39–10.28 km	9.45–13.13 km	10.26–14.27 km
kT_{BB} (keV) ^d	3.05±0.08	2.93±0.07	2.91±0.06
N_{BB} ^e	0.077±0.007	0.077±0.005	0.077±0.005
Γ_{pl} ^f	2.96±0.29	2.97±0.31	3.09±0.08
N_{pl} ^g	5.99±4.01	4.33±2.12	8.53±2.13
E_{Fe} (keV) ^h	6.7	6.7	6.7
σ_{Fe} (keV) ⁱ	0.86±0.29	0.82±0.40	0.88±0.39
N_{Fe} ^j	0.02±0.007	0.019±0.008	0.019±0.009
DiskBB flux	0.50±0.07	0.56±0.06	0.56±0.06
bbody flux	0.62±0.06	0.61±0.05	0.62±0.04
Powerlaw flux	0.39±0.04	0.33±0.04	0.33±0.04
Total flux	1.54±0.01	1.53±0.01	1.53±0.01
L_{3-50}	3.10 ± 0.02	3.08 ± 0.02	3.08± 0.02
\dot{m}	1.66 ± 0.01	1.65 ± 0.01	1.65 ± 0.01
χ^2/dof	47.44/37	42.60/37	41.77/37
χ^2/dof (without Gaussian)	79.12/39	71.40/39	73.59/39
χ^2/dof (without power-law)	155.14/39	118.78/39	324.97/39
F-test (Gaussian) prob.	7.76×10^{-5}	7.09×10^{-5}	2.81×10^{-5}
F-test (Powerlaw) prob.	3.02×10^{-10}	5.77×10^{-9}	3.28×10^{-17}

^aTemperature of the DiskBB model. ^bNormalization of the DiskBB model. ^cEffective radius obtained by using DiskBB Normalization and the spectral correction 1.18–1.64. ^dTemperature of the BB model. ^eNormalization of the BB model. ^fPowerlaw index. ^gNormalization of the PL model. ^hLine energy of the Gaussian model for iron line. ⁱLine width of the Gaussian model for iron line. ^jNormalization of the Gaussian model for iron line.

studies have shown that the causative factor for these large lags could only be the readjustment of the coronal structure, especially since here the inner disk radius is found to be almost at the last stable orbit at all times along the HID (for a detail spectral modeling see Agrawal *et al.* 2020), ruling it out as the agent for change causing the large CCF lags. All the lags were found in the HB and NB. Sriram *et al.* (2019), derived the equation (shown below) for determining the height of the coronal structure based on the condition that the CCF lags are the readjustment timescale of the corona.

$$H_{\text{corona}} = \left[\frac{t_{\text{lag}} \dot{m}}{2\pi R_{\text{disk}} H_{\text{disk}} \rho} - R_{\text{disk}} \right] \times \beta \text{ cm.} \quad (3)$$

Here $H_{\text{disk}} = 10^8 \alpha^{-1/10} \dot{m}_{16}^{3/20} R_{10}^{9/8} f^{3/20}$ cm, $\rho = 7 \times 10^{-8} \alpha^{-7/10} \dot{m}_{16}^{11/20} R_{10}^{-15/8} f^{11/20}$ g cm^{-3} , $f = (1 - (R_s/R)^{1/2})^{1/4}$ and $\beta = v_{\text{corona}}/v_{\text{disk}}$ (Shakura & Sunyaev 1973; Sriram *et al.* 2019).

For the sections A, B, C and D, the coronal height was constrained to be 98 km, 78 km, 58 km and 104 km (for $\beta = 0.1$) and 489 km, 392 km, 292 km and 519 km for $\beta = 0.5$, for $\beta = 0.1 - 0.5$ (Manmoto *et al.* 1997; Pen *et al.* 2003; McKinney *et al.* 2012), an average R_{disk} estimated from DiskBB normalization for each segment and \dot{m} estimated from the luminosity considering the equation $L = GM\dot{m}/R$. Here α was taken to be 0.1.

The lack of spectral variation among the sections and the presence of lags, along with the detection of inner disk radius almost at the last stable orbit, indicate towards the possibility of a non varying disk front and varying coronal structure, which leads to the conclusion that the mass accretion rate is not the factor causing the source to move along the HID but the varying comptonized corona. This was independently reported by Homan *et al.* (2002) and Lin *et al.* (2012), where upon studying GX 17+2 they conclude

Table 6. Same model as used to obtain Table 4 and Best-fit spectral parameters for sections which exhibited HBOs using NthComp + Gaussian + Power-law model. The flux in units of 10^{-8} ergs cm^{-2} s^{-1} is calculated in the energy band 3–50 keV. Errors are quoted at a 90% confidence level. Luminosity is in units of 10^{38} erg s^{-1} , assuming the distance 13 kpc for GX 17+2. Mass accretion rate is in units of 10^{18} g s^{-1} .

Parameter	For HBO 1	For HBO 2	For HBO 3
Γ_{pl}^a	3.0	3.0	3.0
N_{pl}^b	6.96 ± 0.89	4.88 ± 0.77	4.93 ± 0.74
E_{Fe}^c (keV)	6.7	6.7	6.7
σ_{Fe}^d (keV)	0.88 ± 0.27	0.82 ± 0.26	0.84 ± 0.25
N_{Fe}^e	0.021 ± 0.006	0.020 ± 0.006	0.020 ± 0.004
$\Gamma_{NthComp}^f$	1.72 ± 0.03	1.85 ± 0.02	1.86 ± 0.02
kT_e (keV) ^g	3.31 ± 0.06	3.30 ± 0.05	3.28 ± 0.05
kT_{bb} (keV) ^h	0.55 ± 0.11	0.53 ± 0.09	0.54 ± 0.08
$N_{NthComp}^i$	0.70 ± 0.23	1.03 ± 0.3	1.03 ± 0.3
NthComp flux	1.19 ± 0.05	1.28 ± 0.04	1.28 ± 0.04
Powerlaw flux	0.32 ± 0.05	0.22 ± 0.05	0.23 ± 0.05
Total flux	1.54 ± 0.01	1.53 ± 0.01	1.53 ± 0.01
L_{3-50}	3.10 ± 0.02	3.08 ± 0.02	3.08 ± 0.02
\dot{m}	1.66 ± 0.01	1.65 ± 0.01	1.65 ± 0.01
χ^2/dof	47/38	43/38	44/38
F-test (Gaussian) prob.	3.14×10^{-6}	1.19×10^{-6}	6.74×10^{-7}
F-test (Powerlaw) prob.	1.46×10^{-12}	7.70×10^{-11}	2.39×10^{-11}

the same to address the evolution of the source across the HID. Hard lags suggest that the corona is decreasing in size, supported by most of the observations that hard count rates are often found to be decreasing in the light curves (Figures 2 and 3) and vice-versa for soft lags i.e. corona is increasing in height. However as it can be seen from CCFs that it is not always the scenario and more studies are required in this direction. The decreasing corona size should result in narrow equivalent width of iron line (Kara *et al.* 2019) but similar studies require better spectral resolution.

6. Conclusion

- (1) Based on energy-dependent CCF studies, we detect correlated and anti-correlated soft and hard lags of the order of few tens to few hundred seconds in the HB and NB. We interpret these lags as the readjustment timescales of the compact corona close to the neutron star. These lags constrain the coronal height to few tens to few hundred kms.
- (2) PDS study has led to the detection of HBOs of ~ 25 Hz and ~ 33 Hz, along with their harmonics, which are characteristic features of these type of

sources. Based on the RPM and TLM, we find the inner disk radius to be 10–21 R_g .

- (3) Spectral studies of the segments associated with lags show no significant variation in any of the spectral parameters, though we noticed small variations in fluxes for few sections. The inner disk radius was found to be close to the last stable orbit along the HB–NB/FB, suggesting that the disk is not truncated.
- (4) The lack of variation in the disk front suggests that the contributing factor for the source traversing along the HID could be a variation in the corona or boundary layer. Hence we can conclude that the mass accretion rate is not the primary factor for the movement along the HID. This result is in congruence with that of Homan *et al.* (2002) and Lin *et al.* (2012). The readjustment velocity factor of the corona β could play a significant role in this regard.

Acknowledgements

We thank the referee for the comments that has improved the quality of the paper. K.S. and C.P. acknowledge the financial support of ISRO under AstroSat archival Data utilization program. This

publication uses data from the AstroSat mission of the Indian Space Research Organisation (ISRO), archived at the Indian Space Science Data Centre (ISSDC). K.S. also acknowledges the financial support from SERB CRG program. M.S. acknowledges the financial support from DST-INSPIRE fellowship. V.K.A. thanks GH SAG; DD PDMSA, and Director URSC for encouragement and continuous support to carry out this research. Authors sincerely acknowledge the contribution of the LAXPC team toward the development of the LAXPC instrument on-board the AstroSat. This work uses data from the LAXPC instruments developed at TIFR, Mumbai, and the LAXPC POC at TIFR is thanked for verifying and releasing the data via the ISSDC data archive. Authors thank the AstroSat Science Support Cell hosted by IUCAA and TIFR for providing the LAXPC software that was used for LAXPC data analysis.

References

Agrawal V. K., Nandi A., Ramadevi M. C., 2020, *Ap&SS*, 365, 41
 Alpar M. A., Shaham J. 1985, *Nature*, 316, 239
 Antia H. M., Yadav J. S., Agrawal P. C. *et al.* 2017, *ApJS*, 231, 10
 Cackett E. M. *et al.* 2008, *ApJ*, 674, 415
 Cackett E. M. *et al.* 2009, *ApJ*, 690, 1847
 Cackett E. M., Miller J. M., Ballantyne D. R. *et al.* 2010, *ApJ*, 720, 205
 Davis S. W., Blaes O. M., Hubeny I., Turner N. J. 2005, *ApJ*, 621, 372
 Fortner B., Lamb F. K., Miller G. S. 1989, *Nature*, 342, 775
 Galloway D. K., Muno M. P., Hartman J. M., Psaltis D., Chakrabarty D. 2008, *ApJS*, 179, 360
 Hasinger G., van der Klis M. 1989, *A&A*, 225, 79
 Hasinger G., van der Klis M., Ebisawa K., Dotani T., Mitsuda K. 1990, *A&A*, 235, 131
 Homan J., van der Klis M., Jonker P. G. *et al.* 2002, *ApJ*, 568, 878
 Kara E. *et al.* 2019, *Nature*, 565, 198
 Kuulkers E., van der Klis M., Oosterbroek T., Asai K., Dotani T., van Paradijs J., Lewin W. H. G. 1994, *A&A*, 289, 759
 Kuulkers E., van der Klis M., Oosterbroek T., van Paradijs J., Lewin W. H. G. 1997, *MNRAS*, 287, 495
 Kubota A., Tanaka Y., Makishima K., Ueda Y., Dotani T., Inoue H., Yamaoka K. 1998, *PASJ*, 50, 667
 Lamb F. K. 1989, in Hunt J., Battrick B., eds, *Proceedings of the 23rd ESLAB Symposium on Two Topics in X-Ray*

Astronomy, Vol. 1: X Ray Binaries, Vol. 2: AGN and the X Ray Background, ESA, Noordwijk, p. 215
 Lei Y. J., Qu J. L., Song L. M. *et al.* 2008, *ApJ*, 677, 461
 Lin D., Remillard R. A., Homan J. 2007, *ApJ*, 667, 1073
 Lin D., Remillard R. A., Homan J., Barret D. 2012, *ApJ*, 756, 34
 Ludlam R. M. *et al.* 2017, *ApJ*, 836, 140
 Malu S., Sriram K., Agrawal V. K. 2020, *MNRAS*, vol. 499, Issue 2 (2009.11002v2)
 Manmoto T., Mineshige S., Kusunose M. 1997, *ApJ*, 489, 791
 McKinney J. C., Tchekhovskoy A., Blandford R. D. 2012, *MNRAS*, 423, 3083
 Mitsuda K., Inoue H., Koyama K. *et al.* 1984, *PASJ*, 36, 741
 Miyamoto S., Kimura K., Kitamoto S., Dotani T., Ebisawa K. 1991, *ApJ*, 383, 784
 Osherovich, V., Titarchuk, L. 1999a, *ApJL*, 522, 113
 Osherovich, V., Titarchuk, L. 1999b, *ApJL*, 523, 73
 Pen U.-L., Matzner C. D., Wong S. 2003, *ApJ*, 596, L207
 Penninx W., Lewin W. H. G., Zijlstra A. A. *et al.* 1988, *Nature*, 336, 146
 Priedhorsky W., Hasinger G., Lewin W. H. G., Middleditch J., Parmar A., Stella L., White N. 1986, *ApJ*, 306, L9
 Psaltis *et al.* 1999, *ApJ*, 520, 763
 Shakura N. I., Sunyaev R. A. 1973, *A&A*, 24, 337
 Shimura T., Takahara F. 1995, *ApJ*, 445, 780
 Sriram K., Agrawal V. K., Pendharkar J. K., Rao A. R. 2007, *ApJ*, 661, 1055
 Sriram K., Agrawal V. K., Rao A. R. 2009, *RAA*, 9, 901
 Sriram K., Rao A. R., Choi C. S. 2012, *A&A*, 541, A6
 Sriram K., Malu S., Choi C. S. 2019, *ApJS*, 244, 5S
 Stella L., Vietri M. 1999, *Phys. Rev. Lett.*, 82, 17
 Stella L., Vietri M., Morsink S.M. 1999, *ApJL*, 524, 63
 Titarchuk L., Bradshaw C. F., Geldzahler B. J., Fomalont E. B. 2001, *ApJ*, 555, 45
 Titarchuk L. G., Osherovich V. A. 1999, *ApJL*, 518, 95
 van der Klis M. 2006, in Lewin W., van der Klis M., eds, *Compact Stellar X-ray Sources*, Cambridge Univ. Press, Cambridge, p. 39
 van der Klis M. 1988, in Ogelman H., van den Heuvel E. P. J., eds, *NATO Advanced Science Institutes (ASI) Series C*, Vol. 262, NATO Advanced Science Institutes (ASI) Series C, p. 27
 Vaughan B. A., van der Klis M., Lewin W. H. G., van Paradijs J., Mitsuda K., Dotnai T. 1999, *A&A*, 343, 197
 Vrtillek S. D., Raymond J. C., Garcia M. R. *et al.* 1990, *A&A*, 235, 162
 White N. E., Peacock A., Hasinger G., Mason K. O., Manzo G., Taylor B. G., Branduardi-Raymont G. 1986, *MNRAS*, 218, 129
 Wijnands R. *et al.* 1997, *ApJ*, 490, L157
 Wu, X. B. 2001, *ApJ*, 552, 227
 Yadav J. S., Agrawal P. C., Antia H. M. 2016, *Proc. SPIE*, 9905, 99051D
 Zdziarski A. A., Johnson W. N., Magdziarz P. 1996, *MNRAS*, 283, 193